Enhanced charge transfer by phenyl groups at a rubrene/C_{60} interface

Weiwei Mou,[1] Satoshi Ohmura,[1,2] Shinnosuke Hattori,[1] Ken-ichi Nomura,[1] Fuyuki Shimojo,[1,2] and Aiichiro Nakano[1]
[1]*Collaboratory for Advanced Computing and Simulations, Department of Physics & Astronomy, Department of Computer Science, Department of Chemical Engineering & Materials Science, University of Southern California, Los Angeles, California 90089-0242, USA*
[2]*Department of Physics, Kumamoto University, Kumamoto 860-8555, Japan*

(Received 8 January 2012; accepted 23 April 2012; published online 11 May 2012)

Exciton dynamics at an interface between an electron donor, rubrene, and a C_{60} acceptor is studied by nonadiabatic quantum molecular dynamics simulation. Simulation results reveal an essential role of the phenyl groups in rubrene in increasing the charge-transfer rate by an order-of-magnitude. The atomistic mechanism of the enhanced charge transfer is found to be the amplification of aromatic breathing modes by the phenyl groups, which causes large fluctuations of electronic excitation energies. These findings provide insight into molecular structure design for efficient solar cells, while explaining recent experimental observations. © *2012 American Institute of Physics*. [http://dx.doi.org/10.1063/1.4712616]

I. INTRODUCTION

Organic photovoltaic cells have gained great attention because of their potential for lowering the manufacturing cost of solar cells.[1–3] However, the major challenge is their low power conversion efficiency. For increased efficiency, excitons photoexcited in an electron donor material must be rapidly dissociated into electrons and holes at a donor-acceptor interface.[3] Various donor-acceptor interfaces have been studied to identify molecular-design principles for enhanced charge transfer. A prototypical example is rubrene (Rub)/C_{60} and tetracene (Tc)/C_{60},[4] where the only difference between the rubrene and tetracene molecules is the four phenyl groups attached to the aromatic backbone in the former (Fig. 1). Though the electronic energy levels and molecular orbitals responsible for the open-circuit voltage V_{oc} (which is proportional to power conversion efficiency[3]) are similar between rubrene and tetracene, the measured V_{oc}(Rub/C_{60}) is nearly twice as large as V_{oc}(Tc/C_{60}).[4] According to a recent ideal-diode-equation analysis,[5] keys to solving this puzzle are different charge-transfer (CT) and charge-recombination rates between Tc/C_{60} and Rub/C_{60}. Though effects of the phenyl groups in rubrene on the charge-transfer dynamics are speculated to be the origin of this large discrepancy, the atomistic mechanism of the enhanced charge transfer of Rub/C_{60} as compared to Tc/C_{60} remains elusive.

Here, quantum molecular dynamics (QMD) simulation[6] of Rub/C_{60} and Tc/C_{60} interfaces reveals the amplification of breathing modes of aromatic rings by the phenyl groups in rubrene, which results in larger fluctuations of electronic energy levels. Nonadiabatic quantum molecular dynamics (NAQMD) simulation[7–12] shows that this increases the charge-transfer rate at the Rub/C_{60} interface by an order-of-magnitude compared to that at Tc/C_{60}.

II. SIMULATION METHODS

We obtain electronic ground states using the projector-augmented-wave method,[13,14] which is an all-electron electronic-structure-calculation method within the frozen-core approximation in the framework of density functional theory (DFT).[15,16] Projector functions are generated for the 2*s* and 2*p* states of C, and the 1*s* state of H. The generalized gradient approximation (GGA) (Ref. 17) is used for the exchange-correlation energy with nonlinear core corrections.[18] The electronic pseudo-wave functions and the pseudo-charge density are expanded by plane waves with cutoff energies of 30 and 250 Ry, respectively. The energy functional is minimized with respect to Kohn-Sham (KS) orbitals by an iterative method.[19,20] QMD simulations[6] are carried out in the canonical ensemble using the Nose-Hoover thermostat technique.[21,22] The equations of motion are integrated numerically using an explicit reversible integrator[23] with a time step of 20 a.u. (∼0.48 fs). In QMD simulations, interatomic forces are computed quantum mechanically based on the Hellmann-Feynman theorem.

Our QMD code has been implemented on parallel computers by a hybrid approach combining spatial decomposition (i.e., distributing real-space or reciprocal-space grid points among processors) and band decomposition (i.e., assigning the calculations of different KS orbitals to different processors).[24] The program has been implemented using the message passing interface library for interprocessor communications.

We describe excited electronic states within Casida's linear-response time-dependent density functional theory (LR-TDDFT),[9,10,25,26] using the ground-state KS orbitals as a basis set. In LR-TDDFT, electronic excitation energies are calculated from the poles of an electron-hole pair response

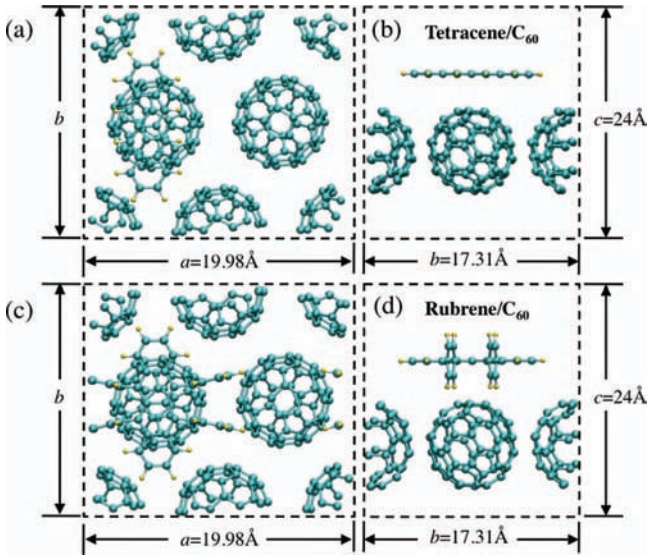

FIG. 1. Top (a) and side (b) views of a tetracene molecule on C_{60} (111) surface, and top (c) and side (d) views of a rubrene molecule on C_{60} (111) surface, where the cyan and yellow spheres represent C and H atoms, respectively.

function. This amounts to solving an eigenvalue problem, with a matrix size of $N_oN_u \times N_oN_u$ when using GGA or $2N_oN_u \times 2N_oN_u$ for hybrid functionals involving the nonlocal Hartree-Fock (HF) exchange potential[27,28] (N_o and N_u, respectively, are the numbers of occupied and unoccupied KS orbitals used to represent excited states). Here, many-body effects[29] are introduced through coupling matrix elements consisting of the random-phase-approximation and exchange-correlation terms.

In order to describe CT excited states, the nonlocal HF exchange potential needs to be taken into account at long distances.[30] We include the long-range exchange correction (LC) through a range-separated hybrid exact exchange functional.[28] The long-range interaction is computed using the reciprocal-space formalism of Martyna and Tuckerman.[31] We adopt a recently proposed non-self-consistent LC approach to reduce the excessive computational cost associated with the exchange integrals.[32]

Figure 2 plots the CT excitation energy calculated by Casida's LR-TDDFT as a function of the distance r between

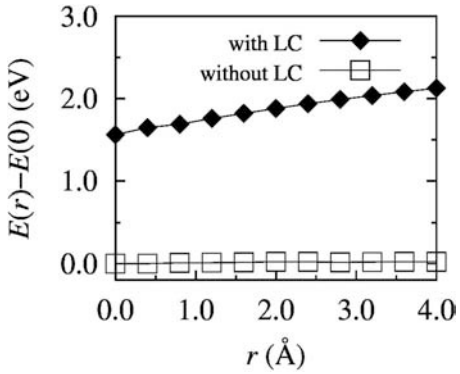

FIG. 2. Charge-transfer excitation energy as a function of the Rub–C_{60} distance. The diamond and square symbols indicate the excitation energies with and without long-range exchange correction (LC), respectively.

Rub and C_{60}. (Here, $r = 0$ signifies the distance for the minimum-energy configuration.) The diamond and square symbols show the excitation energies with and without LC, respectively. The result with LC exhibits the correct asymptotic $-1/r$ behavior.

We perform NAQMD simulations,[7–12] in which transitions between excited electronic states are described by Tully's fewest-switches surface-hopping method.[33] Switching probabilities (or nonadiabatic coupling terms) between excited states are described by a density matrix, and its time evolution is calculated using TDDFT.[34–38] A description of our parallel NAQMD code is found in our previous publication.[11]

In our simulation, one layer of C_{60} is taken from the (111) surface of face-centered-cubic crystal with a lattice constant of 14.13 Å (Fig. 1).[39] A rubrene or tetracene molecule is then placed on top of the center of one C_{60} molecule with the aromatic plane of the rubrene or tetracene parallel to the (111) plane. The distance between the aromatic plane and the C_{60} surface (3.58 and 3.15 Å for rubrene and tetracene, respectively) is determined by minimizing the energy over different distances. The simulation box size is $19.98 \times 17.31 \times 24$ Å^3 for both systems with periodic boundary conditions, where a vacuum layer of thickness ~12 Å is inserted in the [111] direction to prevent the periodic images from interacting. During QMD simulation at a temperature of 300 K, C_{60} centers of mass are constrained to mimic bulk (111) surface.

We have confirmed that the conformations of rubrene and tetracene molecules on the (111) surface of C_{60} face-centered-cubic crystal sampled in our QMD simulations agree with those obtained by larger molecular dynamics (MD) simulations of rubrene and tetracene wetting monolayers on C_{60} (111) surface prepared by a melt-quench procedure. The simulation box of dimensions $68 \times 78 \times 80$ Å^3 contains 320 C_{60} molecules and 30 rubrene molecules (or 72 tetracene molecules), in total of 21 300 atoms (or 21 360 atoms) for the rubrene/C_{60} (or tetracene/C_{60}) system. Periodic boundary conditions are applied to all Cartesian directions, and a vacuum layer of 100 Å is inserted in the z direction (which is parallel to the [111] axis) to prevent the periodic images from interacting. For the classical MD simulations, we use the GROMACS software package[40] and the general Amber force field.[41] The Nose-Hoover thermostat is employed for temparature control during the melt-quench procedure. We first melt rubrene (or tetracene) at a temperature of 700 K on the C_{60} (111) surface. The temperature is then lowered from 700 to 300 K within 1 ns, and the system is thermalized at 300 K for 200 ps. Subsequently, statistical analysis is made for 200 ps, during which MD simulation is performed in the microcanonical ensemble.

Figures 3(a)–3(c) show snapshots of the final MD configurations. The tilt angles α and β defined in Fig. 3(d) describe the conformation of rubrene (or tetracene) molecules on the C_{60} surface. The α and β values averaged over all molecules and time are 11.59° and 4.71° for rubrene molecules, while $\alpha = 7.27°$ and $\beta = 29.89°$ for tetracene molecules. Namely, the aromatic backbones of deposited rubrene and tetracene molecules are nearly parallel to the C_{60} (111) surface, which is consistent with the molecular conformations sampled in our QMD simulation. Similar conformations have been obtained

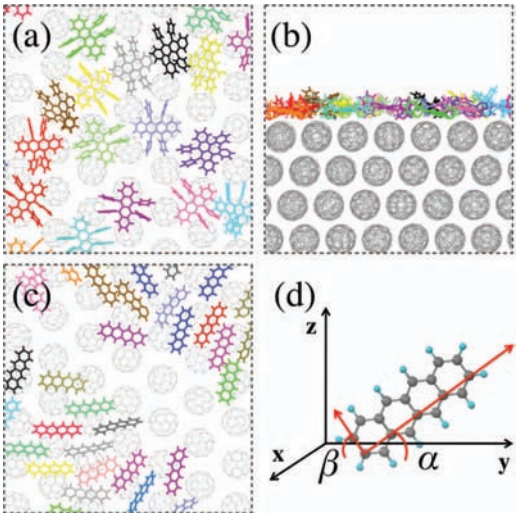

FIG. 3. Top (a) and side (b) views of a zoomed-in snapshot of MD simulation of rubrene molecules (colored lines) on C_{60} (grey lines) (111) surface, where the color is used to distinguish different molecules. (c) A similar snapshot (top view) for tetracene molecules deposited on C_{60} (111) surface. (d) The definition of backbone tilt angles α and β, which are the angles between the xy plane (i.e., the (111) plane of C_{60}) and two vectors that span the backbone plane, respectively.

for MD simulations of low-coverage deposition of pentacene molecules on C_{60} surface.[42]

III. SIMULATION RESULTS

We first confirm that the QMD simulations reproduce the correct electronic band alignment relevant for charge transfer. Photoexcitation of an electron from the highest occupied molecular orbital (HOMO) to the lowest unoccupied molecular orbital (LUMO) in the donor forms a bound electron-hole pair, or exciton. This is followed by charge transfer at the donor-acceptor interface, where the electron is transferred to the acceptor, while the hole remains in the donor. The HOMO and LUMO wave functions of rubrene and tetracene are shown in Fig. 4(a), and their energy level alignment is indicated in Figs. 4(b) and 4(c), which show the time evolution of electronic eigenenergies ε_i of Tc/C_{60} and Rub/C_{60} systems, respectively, during QMD simulation. In Fig. 4, HOMO(α) and LUMO(α) are states with the major probability density in the αth subsystem, where α = Rub, Tc, or C_{60}. The LUMO and HOMO of tetracene or rubrene in Fig. 4(a) are nearly identical to those of an isolated tetracene or rubrene molecule. The band alignment in Figs. 4(b) and 4(c) correctly captures the following key features:

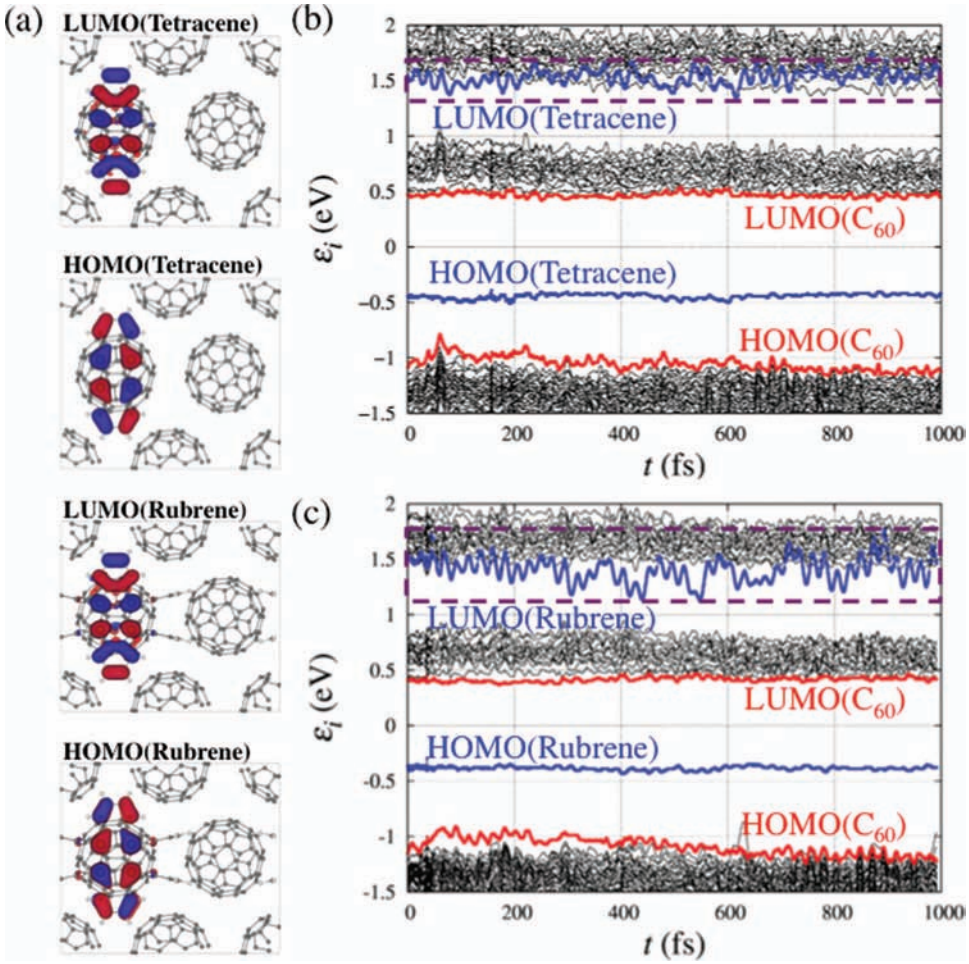

FIG. 4. (a) Spatial distribution of key electronic wave functions in the ground state, where the red and blue isosurfaces correspond to the values of 0.015 and –0.015 a.u., respectively. (b) and (c) show the time evolution of electronic eigenenergies during QMD simulation for the tetracene/C_{60} and rubrene/C_{60} systems, respectively.

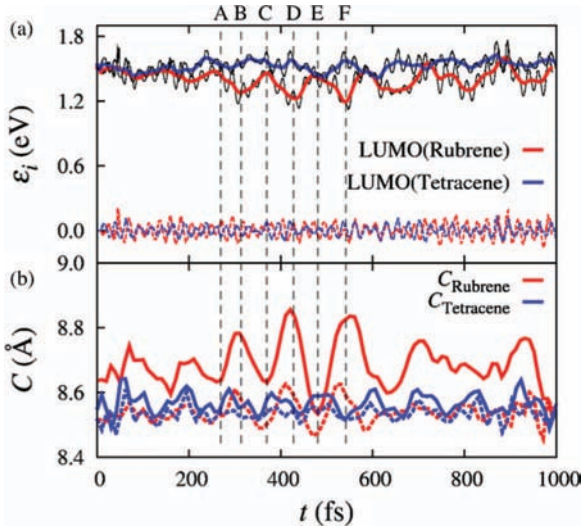

FIG. 5. (a) Time evolution of the LUMO(Rub) and LUMO(Tc) levels (black solid lines) in QMD simulation is decomposed into low-frequency (solid red and blue lines) and high-frequency (dashed red and blue lines) components, respectively. (b) Time evolution of the average circumference of the backbone aromatic rings, where solid and dashed lines are for the middle and end two rings, respectively. The vertical dashed lines mark peaks and valleys labeled A-F.

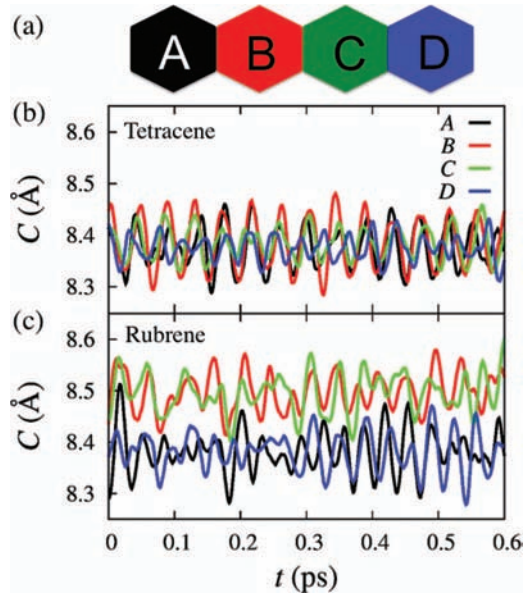

FIG. 6. (a) Schematic of the four aromatic rings A, B, C, and D with the corresponding color code. (b) Time evolution of the circumference $C(t)$ for the four aromatics rings of one of the tetracene molecules in MD simulation. (c) The same as (b) but for rubrene.

(1) HOMO(Tc or Rub) lies between LUMO(C_{60}) and HOMO(C_{60}) (i.e., in the C_{60} band gap), while LUMO(Tc or Rub) falls within the C_{60} conduction band; (2) the C_{60} conduction band is divided into the lowest (T_{1u}) and the next higher (T_{1g}) sub-bands, in agreement with previous theory and experiments;[43] and (3) LUMO(Tc) and LUMO(Rub) are close to the T_{1g} peak and T_{1u}, respectively, in good agreement with experiments, in which LUMO(Tc) and LUMO(Rub) are reported to be 2.1 and 1.3 eV higher than LUMO(C_{60}), respectively.[44,45]

Next, we study how the phenyl groups of rubrene affect the fluctuation of the donor LUMO level. Figure 4(c) shows that the LUMO(Rub) level fluctuates over a much larger energy range (enclosed by dashed purple lines) that bridges the T_{1g} and T_{1u} sub-bands of C_{60}, as compared to LUMO(Tc) that only fluctuates within a narrow energy range in the T_{1g} sub-band. We also note that both LUMO(Rub) and LUMO(Tc) are characterized by rapid fluctuations with a period of 22.7 fs, which in the case of LUMO(Rub) are superimposed with larger-magnitude fluctuations of a longer period of 112 fs.

To identify the molecular origin of the two types of fluctuations, Fig. 5(a) plots LUMO(Rub) and LUMO(Tc) as black solid lines along with their low-frequency components (averaged over a 20 fs window) as solid red and blue lines, respectively. We also plot the time evolution of the circumferences of the backbone aromatic rings of rubrene and tetracene molecules in Fig. 5(b). For Rub/C_{60}, the low-frequency component (the red solid line in (a)) is negatively correlated with the circumferences of the backbone rings (the red lines in (b)). Namely, the peaks labeled A, C, and E of the energy curve coincide with the valleys of the circumference curves, while valleys B, D, and F of the energy curve coincide with the peaks of the circumference curves. The same negative correlation is also present in Tc/C_{60} but with a much smaller magnitude. This identifies the atomistic mechanism of the lower-frequency LUMO(Rub or Tc) energy fluctuations to be the breathing mode of the aromatic rings.

The role of the four phenyl groups in rubrene in promoting the vibration of the backbone rings is partly evidenced by the larger-amplitude breathing of the middle two rings (solid red line in Fig. 5(b)), to which the phenyl groups are attached, compared to that of the end rings (dashed red line in Fig. 5(b)). We have also found that the higher-frequency fluctuations arise from the aromatic C–C stretch mode in the backbone rings, since its period of 22.7 fs is close to that of the aromatic C–C stretch mode at 1500 cm^{-1}. The phenyl groups do not change the frequency of this mode but amplify its magnitude by 50% for rubrene.

To confirm that the amplified breathing modes of the aromatic rings due to the phenyl groups are a generic feature of a rubrene layer deposited on C_{60} surface, Figs. 6(b) and 6(c) plot the circumferences of the four aromatic rings versus time in larger MD simulations of rubrene/C_{60} and tetracene/C_{60}, respectively. The breathing modes of the middle two rings (red and green rings labeled B and C in Fig. 6(a)) in rubrene are significantly amplified with larger average values, as shown by the red and green lines in Fig. 6(c).

The same enhancement of the breathing modes on the middle two rings is also seen in Figs. 7(a) and 7(c), which show Fourier transformed spectra of Figs. 6(b) and 6(c), respectively. Figures 7(b) and 7(d) are close-ups of low-frequency spectra in the frequency range enclosed by dashed lines in Figs. 7(a) and 7(c), respectively. Not only do the two middle rings in rubrene/C_{60} have a higher peak at $\sim$300 cm^{-1} (which corresponds to the longer-period oscillation of $\sim$100 fs discussed above) but they also have increased overall spectral weights in Fig. 7(d).

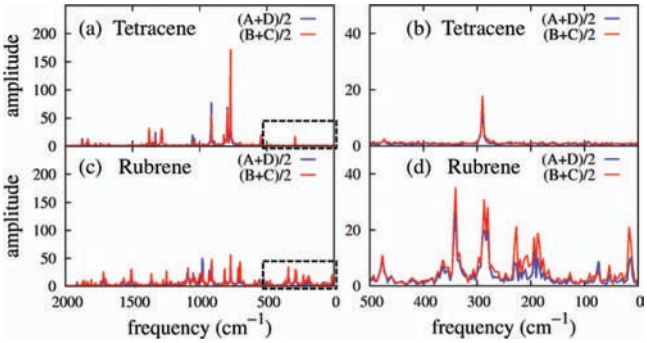

FIG. 7. The vibrational spectrum corresponding to Figs. 6(b) and 6(c), where the blue and red lines are averaged over the two outer and two middle rings, respectively. (a) and (b) are for tetracene, while (c) and (d) are for rubrene. (b) and (d) are close-ups of the low-frequency regions enclosed by the black dashed lines in (a) and (c), respectively.

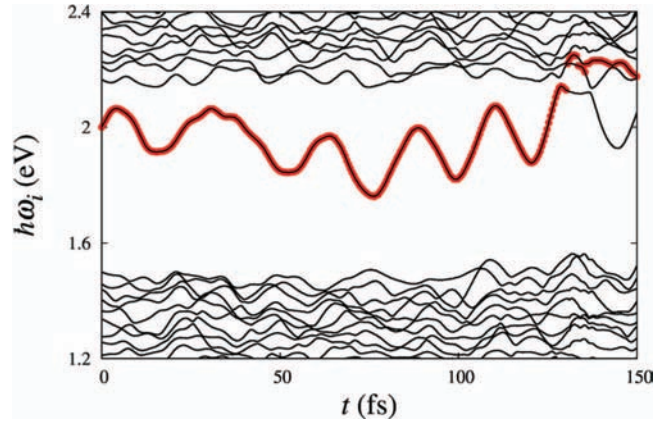

FIG. 9. Time evolution of electronic excitation energies in NAQMD simulation of tetracene/C_{60}. The occupied excited state is indicated by red solid circles. A nonadiabatic transition occurs at about 130 fs.

In order to study how the change of eigenenergy fluctuations due to the phenyl groups affects charge transfer, we perform NAQMD simulation.[7–12] Each NAQMD simulation starts from an electronic excited state corresponding to the excitation of an electron from HOMO(Rub or Tc) to LUMO(Rub or Tc) in an atomic configuration picked from the QMD trajectory. Fifty NAQMD simulations (each for 250 fs) are performed for each of the Rub/C_{60} and Tc/C_{60} systems.

Figure 8 shows the time evolution of key electronic excitation energies along with snapshots of quasi-electron and quasi-hole densities for one of the NAQMD simulations for Rub/C_{60}. We observe larger fluctuations of electronic excitation energies for rubrene than tetracene due to the phenyl groups in the former, which explains why the experimental photoabsorption spectrum of rubrene has wider peaks than that of tetracene.[46] Just after the photoexcitation, both quasi-electron and quasi-hole densities reside within the rubrene as shown in panel A of Fig. 8(a). Between A and B, the atomic configuration relaxes according to the interatomic forces on the excited energy surface, thereby lowering the electronic excitation energy toward the T_{1u} sub-band of C_{60}. Fluctuations of the excitation energy due to the aromatic C–C stretch mode then causes the transfer of the quasi-electron towards the C_{60} side (B and C). Transition from C to D occurs due to the densely populated excitation energies and increased overlap between the electron state and the closest C_{60} state. The charge transfer is completed through a relaxation process from D to E. From E to F is the charge transport process, which involves hopping between localized C_{60} states. The rapid relaxation within ~10 fs indicates that this electron transfer is mediated by aromatic C–C stretching.

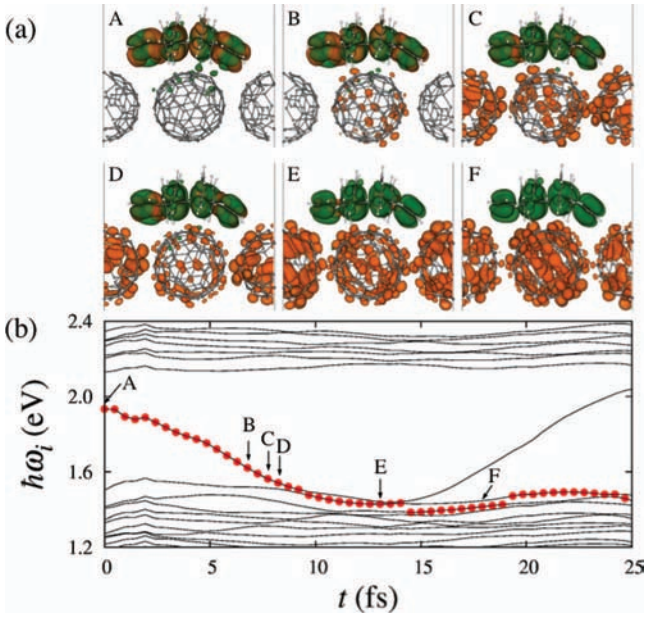

FIG. 8. NAQMD simulation of rubrene/C_{60}. (a) Spatial distribution of exciton charge density at different time steps A-F, where isosurfaces of the quasi-electron and quasi-hole charge densities of 0.015 a.u. are shown in orange and green, respectively. (b) Time evolution of electronic excitation energies. The system is in the excited state indicated by red circles, and the times corresponding to snapshots A-F are indicated by arrows.

Figure 9 shows one event of the charge-transfer process during NAQMD simulation for Tc/C_{60}. The high-frequency fluctuation due to aromatic C–C stretch mode is evident. The transition which occurred at ~130 fs makes the charge transfer from tetracene to C_{60}. The NAQMD simulation for Tc/C_{60} in Fig. 9 exhibits behaviors similar to Fig. 8 but with two notable differences. First, as shown in Fig. 4(b), LUMO(Tc) at the beginning of the NAQMD simulation is closer to the T_{1g} sub-band of C_{60} than in the case of rubrene. Second, fluctuations of excitation energies are smaller, driving the excitation energy away from the T_{1u} sub-band. Accordingly, some charge-transferred excited states only involve the T_{1g} sub-band due to the energy gap between T_{1g} and T_{1u}. In rubrene, a larger relaxation of the excitation energy transfers more quasi-electrons directly to the T_{1u} sub-band, resulting in a faster charge transfer.[4] In fact, in Rub/C_{60}, quasi-electrons in 36 out of 50 NAQMD simulations reach the T_{1u} sub-band within the 250 fs simulation (the rest stay at the bottom of the T_{1g} sub-band). This is in sharp contrast to Tc/C_{60}, where only 8 such events occur out of 50. Following the parallel-replica concept based on first-order kinetics,[47] the average charge-transfer time to the T_{1u} sub-band is estimated to be 155 and 1320 fs in the Rub/C_{60} and Tc/C_{60} systems, respectively.

The amplified long-period (~100 fs) vibration in Rub/C_{60} brings the donor and acceptor energy levels closer

more frequently than in Tc/C_{60} and is essential for enhancing energy-level crossings (which is a prerequisite for charge transfer). Once the energy levels are aligned, however, charge transfer itself occurs at a much shorter time scale (∼10 fs) through nonadiabatic coupling corresponding to C–C stretch. It is also worth noting that the larger fluctuation of electronic energies originating from the phenyl groups is likely to assist the hopping of holes as well. This may partially explain the experimentally observed high hole mobility in rubrene, which is another key factor for higher efficiency.[48]

IV. SUMMARY

In summary, we have performed QMD simulations to determine the atomistic mechanism of charge transfer at rubrene/C_{60} and tetracene/C_{60} interfaces. We found that aromatic breathing and C–C stretch modes play a crucial role in the charge-transfer process. The aromatic breathing modes in rubrene are enhanced by the phenyl groups on the backbone, resulting in enhanced energy-level crossings of LUMO(Rub) with the C_{60} conduction-band levels and an order-of-magnitude larger charge-transfer rate. This may partly explain the higher open-circuit voltage V_{oc}(Rub/C_{60}) compared to V_{oc}(Tc/C_{60}) observed experimentally.[4] The atomistic mechanisms found here shed some light on better molecular structure design for efficient solar cells by promoting key vibrational modes. Such molecular-level considerations should augment calculations of various rates relevant for the power efficiency of solar cells.[49,50]

ACKNOWLEDGMENTS

The work on simulation application was supported by the Center for Energy Nanoscience, an Energy Frontier Research Center funded by the U.S. Department of Energy, Office of Science, Office of Basic Energy Sciences, under Award DE-SC0001013. Performance optimization of the simulation code was supported by the U.S. Department of Energy, SciDAC-e project, under Award DE-FC02-06ER25765. Simulations were performed at the University of Southern California using the 20,925-processor Linux cluster at the High Performance Computing Facility.

[1] M. C. Scharber, D. Wuhlbacher, M. Koppe, P. Denk, C. Waldauf, A. J. Heeger, and C. L. Brabec, Adv. Mater. **18**(6), 789–794 (2006).
[2] J. L. Bredas, J. E. Norton, J. Cornil, and V. Coropceanu, Acc. Chem. Res. **42**(11), 1691–1699 (2009).
[3] C. W. Schlenker and M. E. Thompson, *Topics in Current Chemistry* (Springer, Berlin, 2011), pp. 1–38.
[4] M. D. Perez, C. Borek, S. R. Forrest, and M. E. Thompson, J. Am. Chem. Soc. **131**(26), 9281–9286 (2009).
[5] N. C. Giebink, G. P. Wiederrecht, M. R. Wasielewski, and S. R. Forrest, Phys. Rev. B **82**(15), 155305 (2010).
[6] D. Marx and J. Hutter, *Ab Initio Molecular Dynamics* (Cambridge University Press, Cambridge, England, 2009).
[7] N. L. Doltsinis and D. Marx, Phys. Rev. Lett. **88**(16), 166402 (2002).
[8] C. F. Craig, W. R. Duncan, and O. V. Prezhdo, Phys. Rev. Lett. **95**(16), 163001 (2005).
[9] E. Tapavicza, I. Tavernelli, and U. Rothlisberger, Phys. Rev. Lett. **98**(2), 023001 (2007).
[10] H. Hirai and O. Sugino, Phys. Chem. Chem. Phys. **11**(22), 4570–4578 (2009).
[11] S. Ohmura, S. Koga, I. Akai, F. Shimojo, R. K. Kalia, A. Nakano, and P. Vashishta, Appl. Phys. Lett. **98**(11), 113302 (2011).
[12] X. Zhang, Z. Li, and G. Lu, Phys. Rev. B **84** (23), 235208 (2011).
[13] P. E. Blochl, Phys. Rev. B **50**(24), 17953–17979 (1994).
[14] G. Kresse and D. Joubert, Phys. Rev. B **59**(3), 1758–1775 (1999).
[15] P. Hohenberg and W. Kohn, Phys. Rev. **136**, B864–B871 (1964).
[16] W. Kohn and P. Vashishta, in *Theory of the Inhomogeneous Electron Gas*, edited by N. H. March and S. Lundqvist (Plenum, New York, 1983), pp. 79–147.
[17] J. P. Perdew, K. Burke, and M. Ernzerhof, Phys. Rev. Lett. **77**(18), 3865–3868 (1996).
[18] S. G. Louie, S. Froyen, and M. L. Cohen, Phys. Rev. B **26**(4), 1738–1742 (1982).
[19] G. Kresse and J. Hafner, Phys. Rev. B **49**(20), 14251–14269 (1994).
[20] F. Shimojo, R. K. Kalia, A. Nakano, and P. Vashishta, Comput. Phys. Commun. **140**(3), 303–314 (2001).
[21] S. Nose, Mol. Phys. **52**(2), 255–268 (1984).
[22] W. G. Hoover, Phys. Rev. A **31**(3), 1695–1697 (1985).
[23] M. Tuckerman, B. J. Berne, and G. J. Martyna, J. Chem. Phys. **97**(3), 1990–2001 (1992).
[24] F. Shimojo, S. Ohmura, R. K. Kalia, A. Nakano, and P. Vashishta, Phys. Rev. Lett. **104**(12), 126102 (2010).
[25] M. E. Casida, in *Recent Advances in Density Functional Methods (Part I)*, edited by D. P. Chong (World Scientific, Singapore, 1995), pp. 155–192.
[26] M. Walter, H. Hakkinen, L. Lehtovaara, M. Puska, J. Enkovaara, C. Rostgaard, and J. J. Mortensen, J. Chem. Phys. **128**(24), 244101 (2008).
[27] J. Heyd, G. E. Scuseria, and M. Ernzerhof, J. Chem. Phys. **118**(18), 8207–8215 (2003).
[28] Y. Tawada, T. Tsuneda, S. Yanagisawa, T. Yanai, and K. Hirao, J. Chem. Phys. **120**(18), 8425–8433 (2004).
[29] L. Yang, J. Deslippe, C. H. Park, M. L. Cohen, and S. G. Louie, Phys. Rev. Lett. **103**(18), 186802 (2009).
[30] A. Dreuw, J. L. Weisman, and M. Head-Gordon, J. Chem. Phys. **119**(6), 2943–2946 (2003).
[31] G. J. Martyna and M. E. Tuckerman, J. Chem. Phys. **110**(6), 2810–2821 (1999).
[32] X. Zhang, Z. Li, and G. Lu, J. Phys.: Condens. Matter **24**(20), 205801 (2012).
[33] J. C. Tully, J. Chem. Phys. **93**(2), 1061–1071 (1990).
[34] E. K. U. Gross and W. Kohn, Phys. Rev. Lett. **55**, 2850–2853 (1985).
[35] I. Vasiliev, S. Ogut, and J. R. Chelikowsky, Phys. Rev. Lett. **82**(9), 1919–1922 (1999).
[36] C. Y. Yam, S. Yokojima, and G. H. Chen, Phys. Rev. B **68**(15), 153105 (2003).
[37] S. Meng and E. Kaxiras, J. Chem. Phys. **129**(5), 054110 (2008).
[38] V. Soto-Verdugo, H. Metiu, and E. Gwinn, J. Chem. Phys. **132**(19), 195102 (2010).
[39] Y. J. Guo, N. Karasawa, and W. A. Goddard, Nature (London) **351**(6326), 464–467 (1991).
[40] B. Hess, C. Kutzner, D. van der Spoel, and E. Lindahl, J. Chem. Theory Comput. **4**(3), 435–447 (2008).
[41] J. M. Wang, R. M. Wolf, J. W. Caldwell, P. A. Kollman, and D. A. Case, J. Comput. Chem. **25**(9), 1157–1174 (2004).
[42] L. Muccioli, G. D'Avino, and C. Zannoni, Adv. Mater. **23**(39), 4532–4536 (2011).
[43] E. L. Shirley and S. G. Louie, Phy. Rev. Lett. **71**(1), 133–136 (1993).
[44] C. W. Chu, Y. Shao, V. Shrotriya, and Y. Yang, Appl. Phys. Lett. **86**(24), 243506 (2005).
[45] A. K. Pandey and J. M. Nunzi, Adv. Mater. **19**(21), 3613–3617 (2007).
[46] T. Petrenko, O. Krylova, F. Neese, and M. Sokolowski, New J. Phys. **11**, 015001 (2009).
[47] D. Perez, B. P. Uberuaga, Y. Shim, J. G. Amar, and A. F. Voter, Annu. Rep. Comp. Chem. **5**, 79–98 (2009).
[48] V. Podzorov, E. Menard, A. Borissov, V. Kiryukhin, J. A. Rogers, and M. E. Gershenson, Phys. Rev. Lett. **93**(8), 086602 (2004).
[49] L. W. Wang, Energy Environ. Sci. **2**(9), 944–955 (2009).
[50] Y. Fu, Y. H. Zhou, H. B. Su, F. Y. C. Boey, and H. Agren, J. Phys. Chem. C **114**(9), 3743–3747 (2010).